JOURNAL OF SPACECRAFT AND ROCKETS
Vol. 31, No. 3, May–June 1994

Approximate Method for Calculating Heating Rates on Three-Dimensional Vehicles

H. Harris Hamilton II* and Francis A. Greene†
NASA Langley Research Center, Hampton, Virginia 23681
and
F. R. DeJarnette‡
North Carolina State University, Raleigh, North Carolina 27695

An approximate method for calculating heating rates on three-dimensional vehicles at angle of attack is presented. The method is based on the axisymmetric analog for three-dimensional boundary layers and uses a generalized body-fitted coordinate system. Edge conditions for the boundary-layer solution are obtained from an inviscid flowfield solution, and because of the coordinate system used, the method is applicable to any blunt body geometry for which a inviscid flowfield solution can be obtained. The method is validated by comparing with experimental heating data and with thin-layer Navier-Stokes calculations on the Shuttle Orbiter at both wind-tunnel and flight conditions and with thin-layer Navier-Stokes calculations on the HL-20 at wind-tunnel conditions.

Nomenclature

h = metric coefficient or static enthalpy, m or m^2/s^2
L = vehicle length, m
M = Mach number
p = pressure, N/m^2
q = surface heating rate, W/cm^2
T = temperature, K
t = time, s
Re = Reynolds number, m^{-1}
s = surface distance, m
s, β, n = streamline coordinates (see Fig. 3), m
u, v, w = velocity components, m/s
V = total velocity, m
x, y, z = Cartesian coordinates (see Fig. 1), m
α = angle of attack, deg
β = streamline identifier
ϵ = radius of ϵ circle, m
ϕ = angle between grid lines on surface, deg
γ = ratio of specific heats
τ = time like variable of integration, s/m
ξ, ζ, η = generalized coordinates (see Fig. 2)

Subscripts

nose = nose region
ref = reference
stag = stagnation
x, y, z = derivatives with respect to x, y, z
w = wall
ξ, ζ, η = derivatives with respect to ξ, ζ, η
∞ = freestream

Introduction

THE calculation of aerodymanic heating on advanced entry vehicles is a challenging problem. Configurations of current interest are usually three-dimensional geometries (Fig. 1) that can operate at large angles of attack during periods of peak heating. Because ground-based experimental facilities cannot simulate the real-gas environment of flight, it is necessary to rely heavily on computational fluid dynamic (CFD) flowfield codes to predict the flight environment.

To design these vehicles, it is useful to have both engineering and benchmark computer codes that can be used to predict the aerothermodynamic environment of flight. Engineering codes use approximate numerical methods and descriptions of physical phenomena and are designed to provide reasonably accurate results and to have very fast run times. They can be used to perform the parametric studies required for system design. Benchmark codes use the best available numerical techniques and description of physical phenomena. They provide detailed flowfield predictions, but can require very long run times.

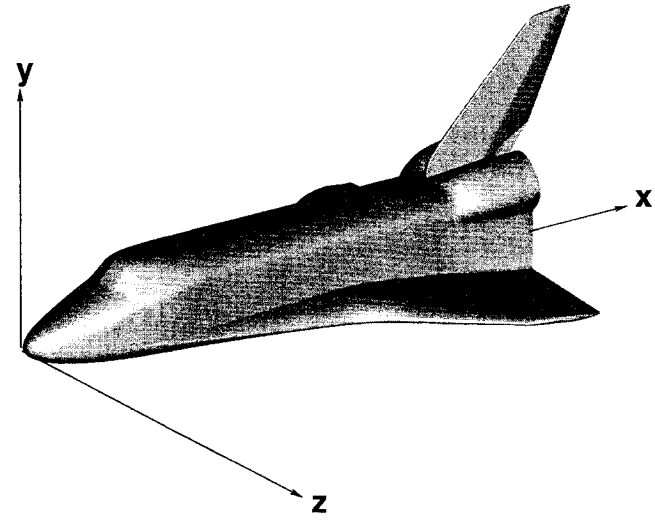

Fig. 1 Shuttle Orbiter geometry.

Received June 22, 1993; presented as Paper 93-2881 at the AIAA 28th Thermophysics Conference, Orlando, FL, July 6–9, 1993; revision received Nov. 24, 1993; accepted for publication Nov. 24, 1993.

*Research Leader, Aerothermodynamics Branch, Space Systems Division. Senior Member AIAA.
†Aerospace Technologist, Aerothermodynamics Branch, Space Systems Division. Member AIAA.
‡Professor, Mechanical and Aerospace Engineering Department. Associate Fellow AIAA.

Hamilton et al.[1] and Weilmuenster and Hamilton[2] developed an engineering method based on the axisymmetric analog[3] for three-dimensional boundary layers that was shown to provide accurate predictions of convective heating rates for vehicles such as blunt cones and a modified Shuttle Orbiter in regions where the flow is attached and the streamline divergence is not too large. Edge conditions for the heating calculations were obtained from a three-dimensional inviscid flowfield solution.[4] In this approach, heating is calculated along individual streamlines. To apply the method, a streamline is chosen and then followed from its origin at the stagnation point until it reaches the end of the body. Then another streamline is chosen and followed from the stagnation point to the end of the body. In principle, proceeding in this fashion, the heating rate over the entire vehicle surface can be calculated. However, in practice this approach is very time consuming to apply because the path that a given streamline would trace out on the body is not known a priori. Large regions of the body (particularly on a wing) are often missed entirely on the first pass, and it becomes very laborious to repeat the process of selecting streamlines, in several passes, until the heating on the entire vehicle is adequately defined. To circumvent this problem, the streamline computing procedure was modified.[5] The modification involved selecting a large number of streamlines that were all computed simultaneously starting immediately downstream of the nose region; then, at each new computational step down the body, the streamlines are redistributed to achieve a more uniform distribution around the body. Thus, the heating over the entire body can be computed in a single pass with no user intervention. This procedure greatly reduces the overall time required to complete a solution. All of the previously cited work, which used spherical coordinates in the nose region and cylindrical coordinates downstream of the nose was coupled to the inviscid flowfield code,[4] which used a similar coordinate system. For the relatively simple geometries, this approach works reasonably well, but it can fail for more complex geometries.

In the present paper, a new engineering method is introduced. The method extends the previous work[1,2,5] to a generalized body-fitted coordinate system.[6] With this new, more general coordinate system, the boundary-layer calculations can be coupled to more general inviscid flowfield solutions,[7] and thus extend the applicability of the heating calculations to almost any vehicle geometry. A complete description of the method is presented, and it is validated by comparison with experimental heating data[8] and with thin-layer Navier-Stokes calculations on the Shuttle Orbiter at both wind-tunnel[8] and flight conditions[9] and with thin-layer Navier-Stokes calculations on the HL-20 at wind-tunnel conditions.

Analysis

In this section, an engineering code (Langley Approximate Three-Dimensional Convective Heating, LATCH) for calculating heating rates on three-dimensional re-entry vehicles is described. First, the discussion focuses on a generalized coordinate system; then on the general nature of the axisymmetric analog and the streamline and metric calculations; next on the method used to solve the boundary-layer equations; and finally on the method of solving the inviscid flowfield and determining the boundary-layer edge properties.

Generalized Coordinate System

To solve the external flowfield over a vehicle, the equations of motion (Euler, Navier-Stokes, boundary layer, etc.) are usually replaced by a set of finite-difference equations that are solved numerically at discrete points within the physical domain of interest surrounding the vehicle. A set of grid points, within the domain as well as on its boundaries, is then constructed in such a way that one of the boundaries of the domain is coincident with the vehicle's surface. This choice makes the specification of boundary conditions much easier. Using this grid, an evenly spaced computational coordinate system ξ, ζ, η can be defined, with the following general transformation equations:

$$\xi = \xi(x, y, z) \tag{1}$$

$$\zeta = \zeta(x, y, z) \tag{2}$$

$$\eta = \eta(x, y, z) \tag{3}$$

Similarly, inverse transformations can be defined as follows:

$$x = x(\xi, \zeta, \eta) \tag{4}$$

$$y = y(\xi, \zeta, \eta) \tag{5}$$

$$z = z(\xi, \zeta, \eta) \tag{6}$$

Because one of the boundaries ($\eta = 0$) of the coordinate system is coincident with the vehicle surface (see Fig. 2), it is referred to as body-fitted. The computational coordinates are evenly spaced; thus, the inverse transformation derivatives x_ξ, x_ζ, x_η, y_ξ, y_ζ, y_η, z_ξ, z_ζ, z_η can be easily computed numerically using central differences. Then the transformation derivatives ξ_x, ξ_y, ξ_z, ζ_x, ζ_y, ζ_z, η_x, η_y, η_z can be computed from the following algebraic equations[6]:

$$\xi_x = J(y_\eta z_\zeta - y_\zeta z_\eta) \tag{7}$$

$$\xi_y = J(x_\zeta z_\eta - x_\eta z_\zeta) \tag{8}$$

$$\xi_z = J(x_\eta y_\zeta - x_\zeta y_\eta) \tag{9}$$

$$\zeta_x = J(y_\xi z_\eta - y_\eta z_\xi) \tag{10}$$

$$\zeta_y = J(x_\eta z_\xi - x_\xi z_\eta) \tag{11}$$

$$\zeta_z = J(x_\xi y_\eta - x_\eta y_\xi) \tag{12}$$

$$\eta_x = J(y_\zeta z_\xi - y_\xi z_\xi) \tag{13}$$

$$\eta_y = J(x_\xi z_\zeta - x_\zeta z_\xi) \tag{14}$$

$$\eta_z = J(x_\zeta y_\xi - x_\xi y_\zeta) \tag{15}$$

Where J is the Jacobian of the transformation defined by

$$J = \frac{\partial(\xi, \zeta, \eta)}{\partial(x, y, z)} = \frac{1}{x_\xi(y_\eta z_\zeta - y_\zeta z_\eta) - x_\eta(y_\xi z_\zeta - y_\zeta z_\xi) + x_\zeta(y_\xi z_\eta - y_\eta z_\xi)} \tag{16}$$

The calculation of the inviscid streamline paths and metrics that describe the convergence/divergence of streamlines are carried out in this coordinate system (ξ, ζ, η). The grid system in physical space required to define this computational space is obtained from the inviscid flowfield solution and is read as an input file before the heating calculations are begun. This type

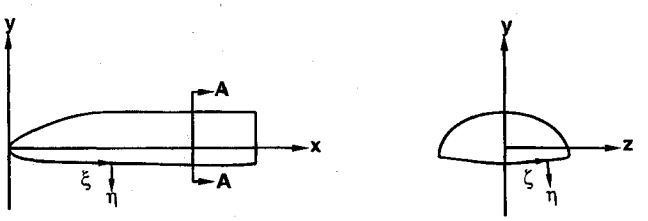

a) Side view. b) Cross Section A-A.

Fig. 2 Generalized coordinate system.

of coordinate system is much more general than the combined spherical–cylindrical system,[1,2,5] and the new system allows the computation of heating over any vehicle geometry for which an inviscid flowfield can be computed.

The vehicle geometry is contained in the grid file read in from the inviscid solution. The vehicle surface is the coordinate surface where $\eta = 0$. Thus, the physical coordinates of the surface can be obtained by setting $\eta = 0$ [see Eqs. (4–6)].

Axisymmetric Analog

Following the approach of Cooke,[3] the general three-dimensional boundary-layer equations are first written in a streamline oriented coordinate system (s, β, n) where s is measured along an inviscid surface streamline, β is tangent to the surface and normal to the streamline direction, and n is normal to the surface (see Fig. 3). If the crossflow velocity in the boundary layer is small, as it is when the wall is cold or when the streamline curvature is small,[1] then it can be neglected. Under this condition, the boundary-layer equations reduce to the same form as for axisymmetric flow provided that the distance along a streamline is interpreted as distance along an equivalent axisymmetric body and that the metric h that describes the convergence/divergence of streamlines is interpreted as the radius of the equivalent axisymmetric body. This simplifies the viscous problem and allows the calculation of approximate three-dimensional heating rates on a body along individual streamlines using any axisymmetric boundary-layer method.

Inviscid Surface Streamlines and Metrics

Before the heating-rate calculation can start, the grid from the inviscid flowfield solution is input as an ordered set of Cartesian coordinates (x, y, z) that is body fitted; i.e., one boundary of the physical grid is coincident with the body surface. The Cartesian velocity components (u, v, w) and thermodynamic variables (p and h) at these grid points are input in a similar manner. The calculation of both the streamlines and metrics needed for the heating predictions are carried out in the computational space (ξ, ζ, η). The physical space is related to the computational space through the inverse transformation Eqs. (4–6). The velocity components (u, v, w) and thermodynamic variables (p and h) can be expressed as functions of the computational coordinates by equations of the following general form:

$$u = u(\xi, \zeta, \eta) \tag{17}$$

$$v = v(\xi, \zeta, \eta) \tag{18}$$

$$w = w(\xi, \zeta, \eta) \tag{19}$$

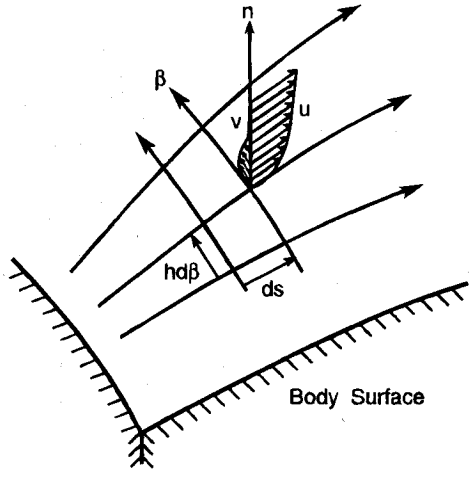

Fig. 3 Typical surface streamlines and boundary-layer velocity profile.

$$p = p(\xi, \zeta, \eta) \tag{20}$$

$$h = h(\xi, \zeta, \eta) \tag{21}$$

The actual calculation of the physical variables in Eqs. (4–6) and Eqs. (17–21) at any general point in the flowfield is accomplished using a standard three-dimensional interpolation scheme.

Nose Region

In the nose region, the coordinates (ξ and ζ) of the inviscid surface streamlines are computed by integrating the following set of differential equations from near the stagnation point:

$$\frac{D\xi}{D\tau} = h_\zeta[u\xi_x + v\xi_y + w\xi_z] \tag{22}$$

$$\frac{D\zeta}{D\tau} = h_\zeta[u\zeta_x + v\zeta_y + w\zeta_z] \tag{23}$$

where τ is the variable of integration, which is related to the distance along a streamline s by the following equation:

$$\frac{Ds}{D\tau} = Vh_\zeta \tag{24}$$

where V is the total inviscid velocity on the surface,

$$V = [u^2 + v^2 + w^2]^{1/2} \tag{25}$$

and h_ζ is defined by the following equation:

$$h_\zeta = [(x_\zeta)^2 + (y_\zeta)^2 + (z_\zeta)^2]^{1/2} \tag{26}$$

The streamline metric h is determined by integrating the following differential equation along a streamline:

$$\frac{D\ ln|h|}{D\tau} = (\bar{\beta}_x[-g_1u_\xi + g_2u_\zeta] + \bar{\beta}_y[-g_1v_\xi + g_2v_\zeta] + \bar{\beta}_z[-g_1w_\xi + g_2w_\zeta])/\sin\phi Vh_\xi G \tag{27}$$

where ϕ is the angle between the coordinates on the surface given by the following equation:

$$\phi = a\cos[(x_\xi x_\zeta + y_\xi y_\zeta + z_\xi z_\zeta)/h_\xi h_\zeta] \tag{28}$$

and h_ξ, g_1, g_2, $\bar{\beta}_x$, $\bar{\beta}_y$, $\bar{\beta}_z$, and G are defined by the following equations:

$$h_\xi = [(x_\xi)^2 + (y_\xi)^2 + (z_\xi)^2]^{1/2} \tag{29}$$

$$g_1 = \left(\frac{\partial \boldsymbol{R}}{\partial \zeta}\cdot \boldsymbol{V}\right) = x_\zeta u + y_\zeta v + z_\zeta w \tag{30}$$

$$g_2 = \left(\frac{\partial \boldsymbol{R}}{\partial \xi}\cdot \boldsymbol{V}\right) = x_\xi u + y_\xi v + z_\xi w \tag{31}$$

$$\bar{\beta}_x = -[x_\xi g_1 - x_\zeta g_2] \tag{32}$$

$$\bar{\beta}_y = -[y_\xi g_1 - y_\zeta g_2] \tag{33}$$

$$\bar{\beta}_z = -[z_\xi g_1 - z_\zeta g_2] \tag{34}$$

and

$$G = \sqrt{(\bar{\beta}_x)^2 + (\bar{\beta}_y)^2 + (\bar{\beta}_y)^2} \tag{35}$$

respectively.

The streamline and metric [Eqs. (22–24), and (27)] are singular at the stagnation point and the nose point ($x = 0$), and care must be exercised when integrating the equations in the region near these points. The use of τ instead of s as the variable of integration helps control some of the problems associated with these singularities, because it helps to automatically control the integration step size in physical space ds near these points. Because $V \to 0$ at the stagnation point and $h_\xi \to 0$ at the nose point, $Ds/D\tau$ also $\to 0$ near these points [see Eq. (24)], and the integration of the differential equations proceeds more smoothly in these regions.

To start the calculation for a streamline, the stagnation point is first located from the inviscid flowfield data, and then a small circle of radius ϵ is drawn on the surface surrounding the stagnation point. The streamline calculation begins on this circle (to avoid the stagnation point singularity), and the streamline is identified by the meridional angle β, where it crosses the circle. For a positive angle of attack, $\beta = -90$ deg identifies the streamline that travels along the windward symmetry plane, and $\beta = +90$ deg identifies the streamline that first travels forward along the windward symmetry plane toward the nose, through the nose point, and then along the leeward symmetry plane.

The solution for the nose region is obtained by selecting a series of streamlines and successively integrating the differential equations for the streamline path and metric [Eqs. (22–24) and (27)] for each of these streamlines from the stagnation point to a constant preselected ξ-station downstream where $\xi > \xi_{stag}$.

Region Downstream of Nose

In the downstream region, the independent variable of integration is changed from τ to ξ for convenience, and the remaining coordinate defining the streamline location on the surface (ζ) and the surface distance (s) are computed by integrating the following set of differential equations along each streamline:

$$\frac{D\zeta}{D\xi} = \frac{\zeta_x u + \zeta_y v + \zeta_w w}{\xi_x u + \xi_y v + \xi_z w} \tag{36}$$

$$\frac{Ds}{D\xi} = \frac{V}{\xi_x u + \xi_y v + \xi_z w} \tag{37}$$

The streamline metric h is determined by integrating the following differential equation along a streamline:

$$\frac{D \ln|h|}{D\xi} = [\bar{\beta}_x(-g_1 u_\xi + g_2 u_\zeta) + \bar{\beta}_y(-g_1 v_\xi + g_2 v_\zeta) + \bar{\beta}_z(-g_1 w_\xi + g_2 w_\zeta)]/\sin\phi V h_\xi h_\zeta G] \frac{1}{U_\xi} \tag{38}$$

where V, ϕ, h_ζ, h_ξ, g_1, g_2, $\bar{\beta}_x$, $\bar{\beta}_y$, and $\bar{\beta}_z$, and G are the same as previously defined [see Eqs. (25) and (26) and (28–35)] and U_ξ is the contravariant velocity component normal to a ξ = constant surface given by the following equation:

$$U_\xi = \frac{D\xi}{Dt} = \xi_x u + \xi_y v + \xi_z w \tag{39}$$

Boundary-Layer Solution

With the axisymmetric analog, any axisymmetric boundary-layer method can be applied along an inviscid surface streamline to obtain an approximate three-dimensional boundary-layer solution. In the present paper, surface heating rates are the primary objective. These heating rates can be calculated using a full finite–difference solution of the axisymmetric boundary-layer equations[10]; however, this is not necessary because very accurate heating rates can be obtained with less computational effort using an approximate heating method developed by Zoby et al.[11] This method is valid for both laminar and turbulent flow and has been shown to yield very accurate results (generally within $\pm$ 10%) for both wind tunnel and flight conditions[1,11,12] with only a fraction of the computational effort required for a full boundary-layer solution. This method is used exclusively in the present paper for calculating three-dimensional heating rates, but only the equations for computing laminar heating have been implemented.

Inviscid Flowfield Solution and Boundary-Layer Edge Properties

The method presented in this paper for computing heating over three-dimensional bodies requires that the cartesian grid and velocity field over the entire vehicle be specified in order to calculate the necessary streamline paths and metrics. Although any method could have been used to compute the inviscid flowfield, the method used in this paper is the inviscid version of the Langley Aerothermodynamic Upwind Relaxation Algorithm (LAURA) code.[7] This method has been shown to provide accurate predictions of the flowfield results for a wide range of vehicle geometries and flow conditions. LAURA uses a three-dimensional, finite-volume algorithm, and relaxes the governing equations in pseudotime using a point-implicit technique until the solution reaches steady state.

The boundary-layer edge properties are obtained by interpolating in the inviscid flowfield at a distance equal to the boundary-layer thickness away from the wall.[11] To accomplish this, an initial assumption is made for the boundary-layer edge properties (usually equal to the wall values), and the solution is iterated until the assumed values for the edge properties are equal to the calculated values. This process usually takes two or three iterations to converge. This is the same approach used previously in Refs. 1, 5, 11, and 12. The use of edge properties determined in this manner accounts approximately for the variable boundary-layer-edge entropy effect.

Heating Calculations Over Complete Vehicle

The method that has been described can be applied in two basic procedures to calculate the heating over a vehicle. In the first procedure,[1] the entire vehicle is treated as a "nose region," and the heating is calculated along individual streamlines independent of other streamlines. In this approach, a streamline is selected, and a solution along that streamline is computed from the stagnation point to the end of the body using Eqs. (22–24) and (27). Then another streamline is selected, and the solution is computed along that streamline. This approach works well for simple bodies with relatively simple streamline paths, and it can, in principle, be applied to any body shape. However, for complex bodies with complex streamline paths, this method is very difficult to apply because the streamline path is not known a priori, and large regions of the vehicle (particularly on the wing) are often missed entirely on the first pass (see Fig. 4). It then becomes very laborious to repeat the process of selecting streamlines (usually requiring several passes) until the heating over the entire vehicle is adequately defined.

To circumvent this problem, the procedure outlined in the previous section has been modified.[5] This new procedure involves selecting a set of streamlines as described previously and solving for these streamlines from the stagnation point to a constant ξ-station designated as the end of the nose region ξ_{nose} (where ξ_{nose} is typically located at approximately 10% of the body length). The solution is carried out in such a way as to provide a relatively uniform distribution of streamlines at the end of the nose region. In the "region downstream of the nose," the variable of integration is changed from τ to ξ, and

the solution for all of the streamlines is obtained simultaneously using Eqs. (36–38) in a step-by-step marching fashion until the end of the body is reached. Between each step, the streamlines are "redistributed" i.e., a new set of streamlines is chosen in such a way that a more uniform streamline distribution is maintained (see Fig. 5). Thus, the heating over an entire body can be obtained in one pass with no user intervention. Although this approach increases the time required to solve for a given number of streamlines (or grid points around the body), this method greatly reduces the overall time required to obtain an acceptable heating solution for an entire body. This procedure is used in the present paper.

Note that the computational grid lines for the heating calculations on the lower surface, shown in Fig. 5, bend back toward the lower symmetry plane near the end of the body. This behavior is a consequence of choosing to align the computational grid for heating with the surface grid used in the inviscid computations. Such an anomaly in the computational grid has no direct effect on the accuracy of the heating calculations, but it may have an indirect effect if the accuracy of the inviscid solution is affected. The effect of this grid anomaly on the inviscid solution needs further investigation.

Results and Discussion

In this section, heating predictions from the LATCH code are compared with thin-layer Navier-Stokes calculations and experimental data first on the Shuttle Orbiter at both wind-tunnel and flight conditions and then on the HL-20 at wind-tunnel conditions.

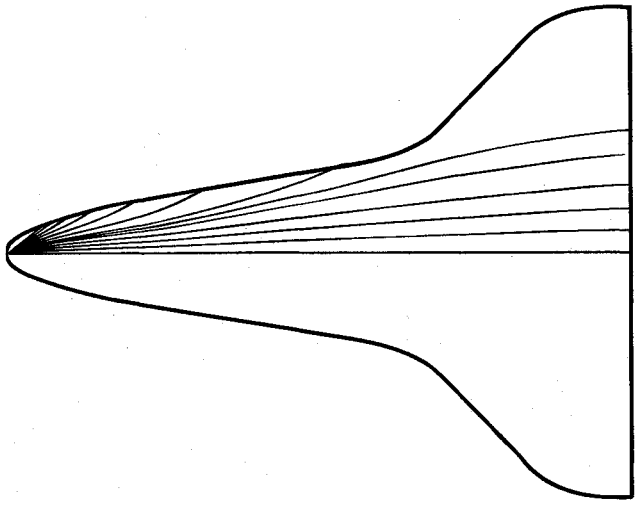

Fig. 4 Typical inviscid surface streamlines on lower surface of Shuttle Orbiter at α = 30 deg.

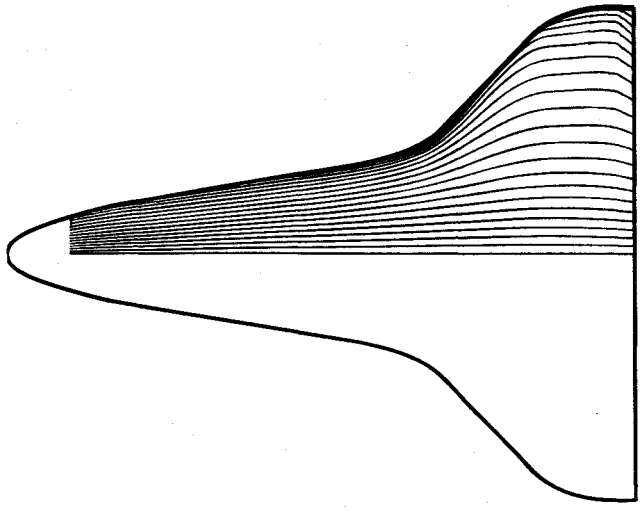

Fig. 5 Typical computational grid for heating calculations on lower surface of Shuttle Orbiter at α = 30 deg using streamline redistribution.

The first comparisons are for the high alpha inviscid solution (HALIS) orbiter configuration, which is shown in Fig. 6 along with the complete Shuttle Orbiter geometry. This geometry model was developed initially for use with the HALIS[4] inviscid flowfield code to simplify flowfield calculations. The HALIS orbiter models the lower surface of the Shuttle Orbiter to a $x/L = 0.94$ and has the same upper symmetry-plane profile as the Shuttle Orbiter (except for canopy and vertical tail). However, the upper surface has been modified by filling in the region between the leading edge of the strake or wing and the upper symmetry plane with elliptical segments. This simplifies the leeside geometry and makes calculations in this region much easier; however it does not affect calculations on the windward side, because at the angles of attack of interest, the crossflow velocity at the leading edge of the lower surface is supersonic.

A 0.0075-scale wind-tunnel model of the HALIS orbiter has been designed and tested at the Langley Research Center.[8] The model was instrumented with many heat-transfer gages that provide reasonably detailed circumferential heating distributions. The case considered is at a Mach number of 5.83 in air (γ = 1.4) and an angle of attack of 30 deg. The freestream flow conditions are given in Table 1, and the flow is assumed to be laminar.

The comparison of heating along the windward symmetry plane is presented in Fig. 7. The results are plotted as q_w vs x/L, where x is the distance along the model axis measured from the nose and L is the model length. The LATCH predictions are in excellent agreement with AA3DBL[5] and the experimental data. Note that AA3DBL used an inviscid flowfield solution obtained from the HALIS inviscid flowfield code.[4] The LAURA[5] heating predictions (thin-layer Navier-Stokes) are slightly higher (approximately 10%) than LATCH for $x/L \leq 0.85$. Further rearward on the body ($x/L \geq 0.85$), the LAURA results are lower than are the other calculations and the experimental data. The grid used in the LAURA calculations for this case may be inadequate to resolve the flow as it expands onto the rearward portion of the model lower surface (see Ref. 5) which probably accounts for the underprediction in this region. However, the results are still in reasonably good agreement with the other data.

Comparison of heating in a circumferential direction around the model is presented in Fig. 8 at an axial station where $x/L = 0.55$. The results are plotted as q_w vs s/L, where s is the surface distance around the model measured normal to the symmetry plane: s starts at the lower symmetry plane and increases toward the upper symmetry plane. In general, the heating first increases in a direction away from the lower symmetry plane; then reaches a peak near the leading edge; and finally decreases rapidly on the leeside. The peak in heating near the leading edge is caused by a strong divergence of the flow in this region. This general pattern of circumferential heating has been observed[5] at all axial stations. The LATCH predictions are in good agreement with the other results near the lower symmetry plane ($s/L = 0$) but are lower than the other results in the vicinity of the leading edge ($s/L \approx 0.125$). LATCH and AA3DBL are very similar codes, and although

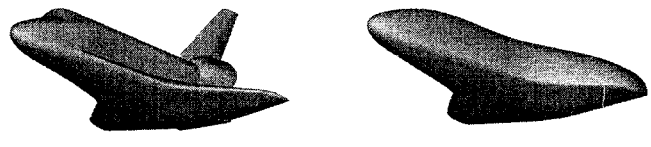

a) Shuttle Orbiter b) "HALIS" Orbiter

Fig. 6 Geometry description; a) Shuttle Orbiter and b) HALIS Orbiter.

Table 1 Freestream flow conditions

Configuration	α, deg	Altitude, km	p_∞, N/m^2	T_∞, K	M_∞	Re, m^{-1}
HALIS	30.0	——	153.2	61.9	5.83	1.94×10^6
Shuttle	34.8	46.7	100.3	260.0	9.15	0.24×10^6
Shuttle	38.3	53.0	50.9	262.0	11.90	0.15×10^6
Shuttle	40.0	54.8	40.0	261.6	12.86	0.15×10^6
HL-20	25.0	——	607.5	63.0	5.93	7.54×10^6

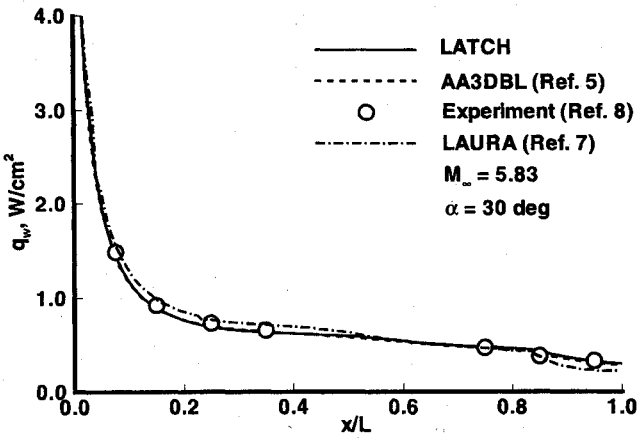

Fig. 7 Windward symmetry-plane heating distribution on HALIS Orbiter.

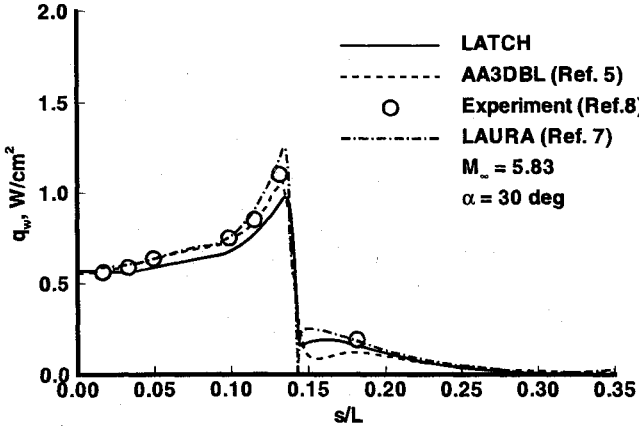

Fig. 8 Circumferential heating distribution on HALIS Orbiter at $x/L = 0.55$.

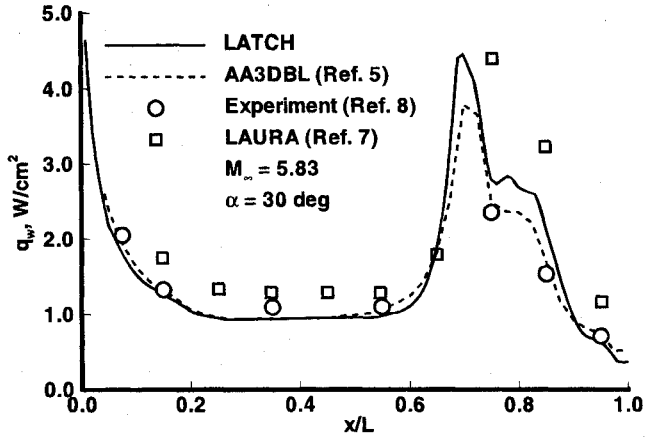

Fig. 9 Maximum heating along wing leading edge of HALIS Orbiter.

they are written in different coordinate systems, they should be expected to produce almost identical results for this case. The primary difference between these two heating predictions is in the inviscid solutions that were used. AA3DBL used inviscid data from the HALIS code, whereas LATCH used data from an inviscid version of the LAURA code. The HALIS code uses a combined spherical/cylindrical coordinate system to describe the flowfield, whereas the inviscid version of the LAURA code uses generalized body-fitted coordinate system that provides a better description of the flowfield for this type of body. Some differences have been noted in the pressures and surface velocities near the leading edge, and it is thought that this probably caused the difference in the predicted heating. The reason for these differences needs further exploration.

The maximum heating rates near the wing (or fuselage) leading edge for this case are presented in Fig. 9 as a function of x/L. The experimental values of heating are shown only for those cross sections where a gauge was located near the leading edge. Note that the experimental measurements, although dense compared with other experimental studies, are probably not sufficiently dense to capture the "absolute maximum" leading-edge heating, and thus the actual peak experimental values are probably higher than those shown. In addition, surface conduction is usually a problem near a small leading edge such as this, and conduction would also tend to reduce the measured heating rates. The rapid rise in heating near $x/L = 0.6$ is associated with the beginning of the wing. The leading-edge heating reaches a sharply defined peak near $x/L = 0.7$, and the peak that approaches the stagnation-point value. This peak in heating is located just downstream of the start of the wing shock (see Ref. 5). Farther downstream, the heating first decreases rapidly; levels out near the start of the bow-shock wing-shock interaction ($x/L = 0.75$); and then decreases rapidly again as the wing turns more parallel to the flow. There are some differences in the LATCH and AA3DBL heating predictions that are thought to be attributable to differences in the inviscid solutions used in each case (see previous paragraph), but both predictions "track" the experimental data reasonably well. The LAURA predictions are higher (30–40%) than the other results over the forward part of the body and are much higher (35–70%) than the other results over the rearward part of the body. These differences over the rearward portion of the body are thought to be the result of inadequate grid resolution in this region, as discussed previously.

Several points on the STS-2 trajectory were analyzed in Ref. 13, and it was concluded that the flow over the windward side of the Shuttle Orbiter in flight remained in chemical nonequilibrium down to an altitude of approximately 50 km. Because, at the present time, LATCH does not include chemical nonequilibrium effects, three STS-2 trajectory points were chosen for analysis where the flow is expected to be near chemical equilibrium. The first is at an altitude of 46.67 km, and the second is at an altitude of 52.97 km, and the third is at an altitude of 54.8 km (see Table 1 for freestream flow conditions). For these cases, heating predictions on the windward side of the Shuttle Orbiter are presented and compared with STS-2 flight data.[9] All of the inviscid data used in LATCH to perform the heating calculations were obtained from an inviscid version of LAURA using a grid with 145 points down the body, 81 points around the body, and 65 points between the body and the outer computational boundary. Each inviscid solution required approximately 5–10 hours of computational time on a Cray Y-MP. Each

LATCH solution was obtained using 201 streamlines and required approximately 20 minutes of computing time on a Sun SPARCstation 10.

For an altitude of 46.7 km, the heating predictions from LATCH along the windward symmetry plane of are presented in Fig. 10 along with the STS-2 flight data[9] for comparison. These calculations assume that the flow is laminar and in chemical equilibrium. There is some apparent scatter in the experimental data, but, in general, the LATCH predictions are in very good agreement with the flight data.

Lateral heating distributions in planes normal to the axis of the Shuttle Orbiter at x/L stations of 0.1, 0.4, 0.5, 0.6, and 0.7 are presented in Figs. 11–15, respectively. The results are plotted as q_w/q_{ref} vs z/L. Again, there seems to be some scatter in the data; but, except for $x/L = 0.5$, the predicted values are in reasonably good overall agreement with the flight data. At $x/L = 0.5$, the two outboard data points are significantly higher than the predicted values. Other investigations (e.g., Refs. 1 and 14) have noted similar "problems" with these two measurements when comparing heating predictions with the shuttle flight data. Examination of the time histories of these two thermocouples shows that they are laminar, and there is nothing unusual about their time traces that would suggest that the thermocouples are bad. The reason for these large differences is unknown.

LATCH heating predictions along the windward symmetry plane for altitudes of 53.0 and 54.8 km (see Table 1) are pre-

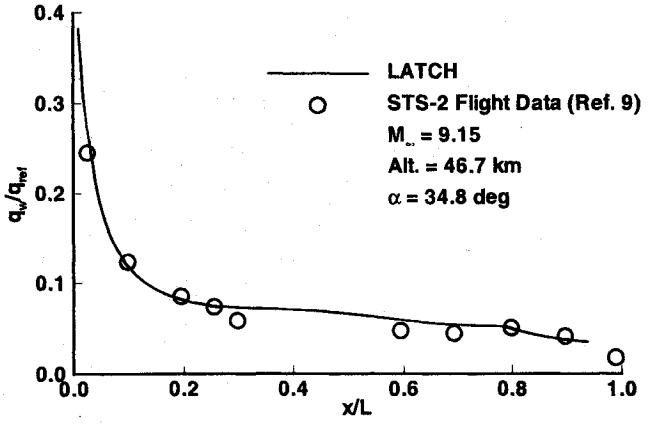

Fig. 10 Windward symmetry-plane heating on Shuttle Orbiter.

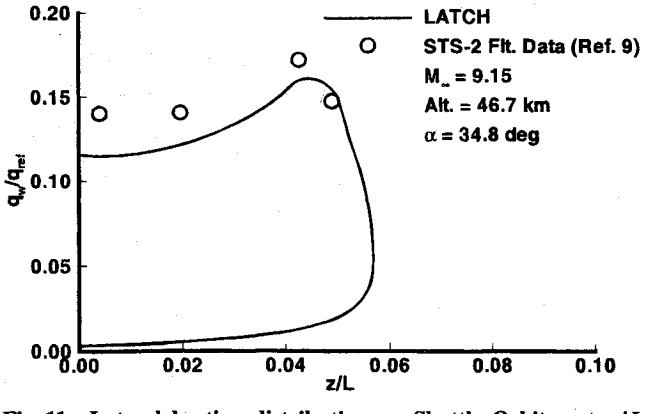

Fig. 11 Lateral heating distribution on Shuttle Orbiter at $x/L = 0.1$.

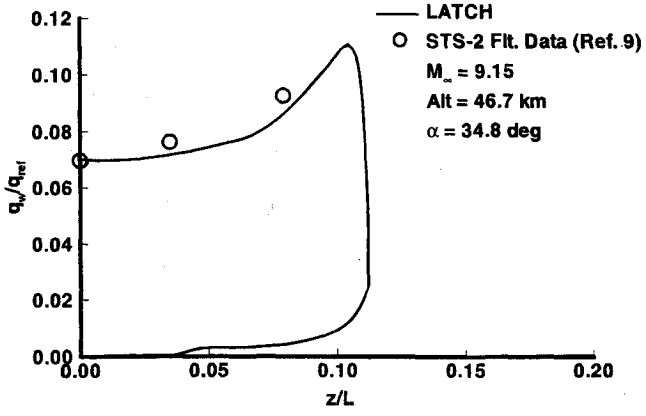

Fig. 12 Lateral heating distribution on Shuttle Orbiter at $x/L = 0.4$.

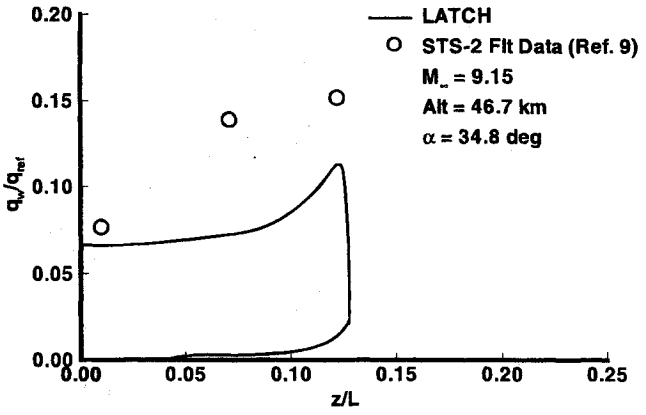

Fig. 13 Lateral heating distribution on Shuttle Orbiter at $x/L = 0.5$.

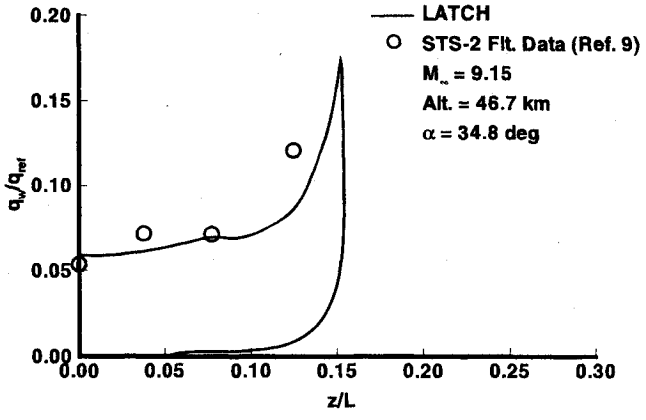

Fig. 14 Lateral heating distribution on Shuttle Orbiter at $x/L = 0.6$.

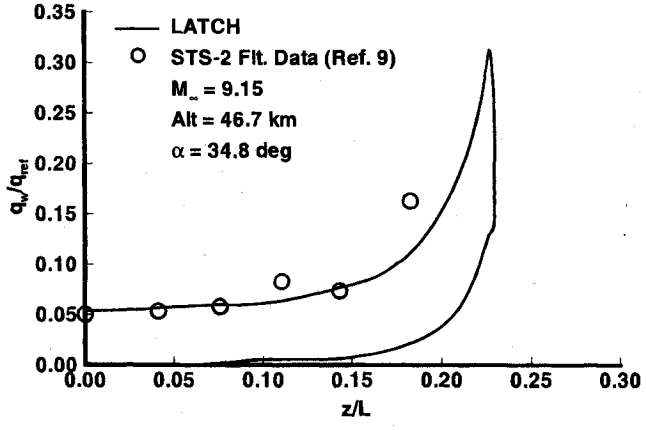

Fig. 15 Lateral heating distribution on Shuttle Orbiter at $x/L = 0.7$.

sented in Figs. 16 and 17, respectively, along with the STS-2 flight data for comparison. The calculations assume that the flow is in chemical equilibrium. When these results are compared with those presented in Fig. 10, it is seen that, as the altitude increases above approximately 50 km, the LATCH results are progressively higher then experimental data (especially over the forward part of the body). This comparison suggests that for altitudes above about 55 km, the flight data are beginning to exhibit chemical nonequilibrium effects, which is the same conclusion reached in Ref. 13.

Heating rate predictions from the LATCH code are also compared with calculations from the LAURA code and limited experimental data on the HL-20 configuration[15] (see Fig. 18), which is being studied as a possible future manned entry vehicle. The flow is assumed to be laminar, and the freestream flow conditions are given in Table 1. All of the inviscid data used in LATCH to perform the heating calculations were obtained from an inviscid version of the LAURA code using a grid 125 points down the body, 81 points around the body, and 47 points between the body and the outer computational boundary. Each

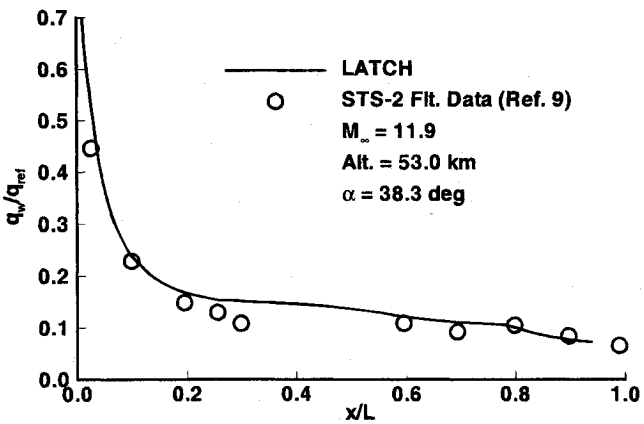

Fig. 16 Windward symmetry-plane heating on Shuttle Orbiter.

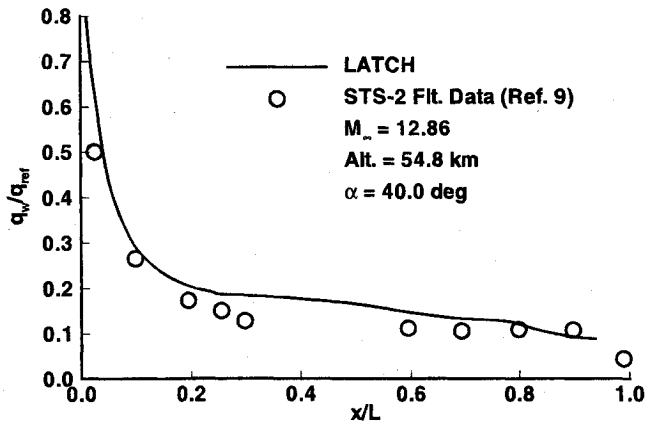

Fig. 17 Windward symmetry-plane heating on Shuttle Orbiter.

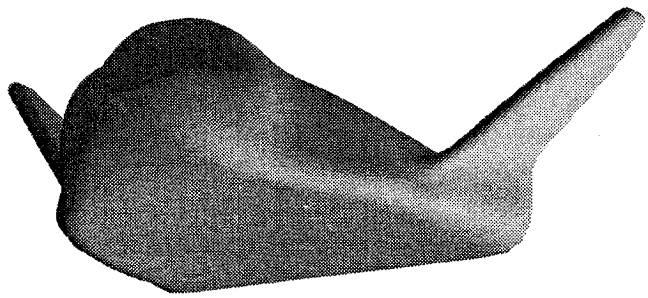

Fig. 18 HL-20 geometry.

inviscid solution required approximately 4–6 hours of computational time on a Cray Y-MP. Each LATCH solution was obtained using up to 301 streamlines and required approximately 10 minutes of computing time on a Sun SPARCstation 10.

The comparison of heating rates along the windward symmetry plane is presented in Fig. 19. The results are plotted as q_w/q_{ref} vs x/L. For the windward symmetry plane, heat transfer data obtained using a thermal phosphor technique are available for comparison. These data were provided by Ron Merski of the Langley Research Center. Also included in Fig. 19 are heating predictions from the thin-layer Navier-Stokes version of the LAURA code. The LATCH results are almost identical to the LAURA results over the forward part of the body, but they are approximately 10 % higher near the end of the body. However, both are in reasonably good agreement with the experimental data.

The comparison of heating rates in a circumferential direction around the model is presented at axial stations of 0.2, 0.4, 0.6, and 0.8. The cross-sectional geometry for these axial stations is presented in Fig. 20. The AA3DBL code,[5] which uses a cylindrical coordinate system, cannot be used to calculate the heating over this geometry because of the complex cross-sectional shape produced by the wings (see $x/L = 0.8$ in Fig. 20). However, the LATCH code, which uses a generalized body-fitted coordinate system discussed previously, can be applied easily.

The circumferential heating distributions for this case are presented in Figs. 21–24. The results are plotted as q_w/q_{ref} vs s/L where s is the surface distance around the body measured normal to the symmetry plane. At $x/L = 0.2$ (Fig. 21), the LATCH predictions are in reasonably good agreement with the LAURA calculations except near the peak that occurs near the

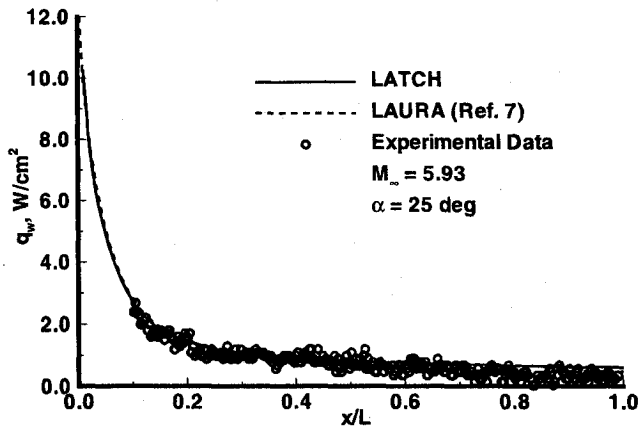

Fig. 19 Windward symmetry-plane heating on HL-20.

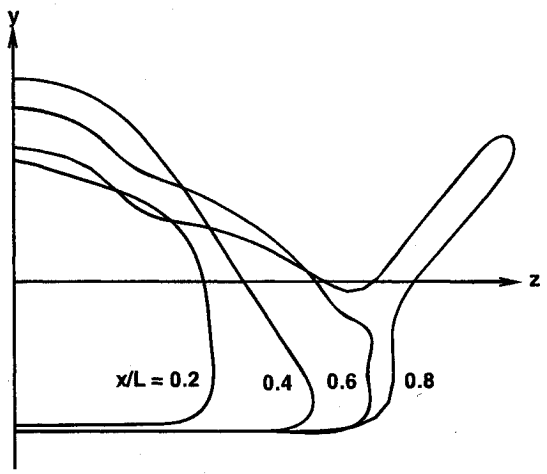

Fig. 20 Cross sectional geometry of HL-20.

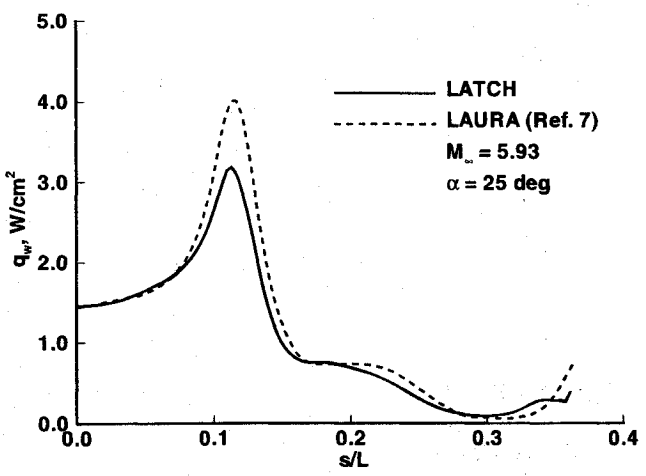

Fig. 21 Circumferential heating distribution on HL-20 at $x/L = 0.2$.

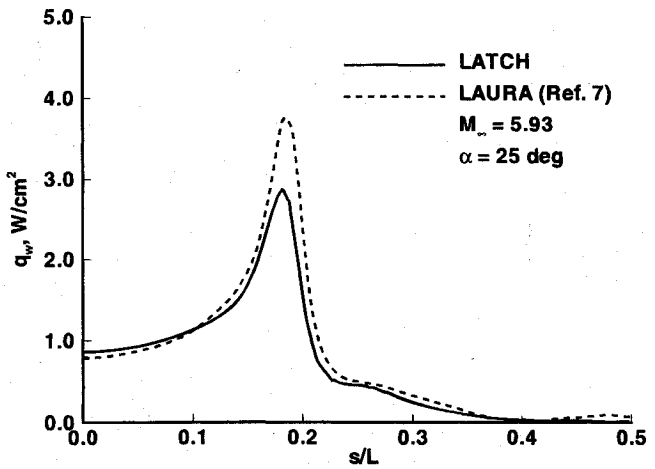

Fig. 22 Circumferential heating distribution on HL-20 at $x/L = 0.4$.

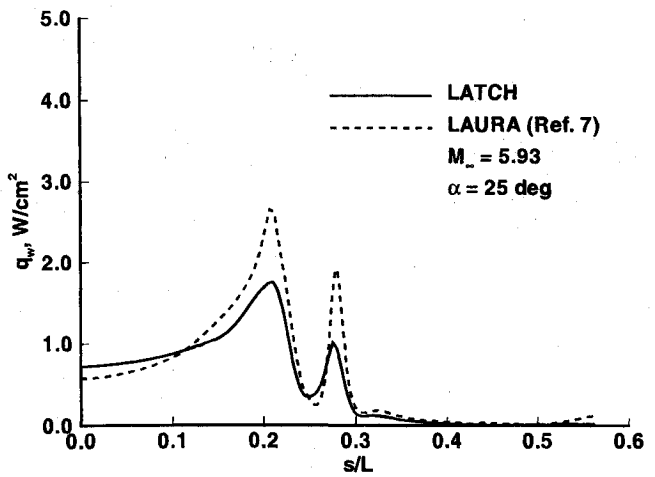

Fig. 23 Circumferential heating distribution on HL-20 at $x/L = 0.6$.

edge of the fuselage lower surface. In this region, the flow near the surface is diverging very rapidly, and thus the three-dimensional effects on heating are large. At $x/L = 0.4$ (Fig. 22), the heating distribution is similar to that at $x/L = 0.2$.

At $x/L = 0.6$ (Fig. 23), the wing is beginning to form (see Fig. 20), and it causes a change in the heating distribution. The heating increases in a direction away from the symmetry plane;

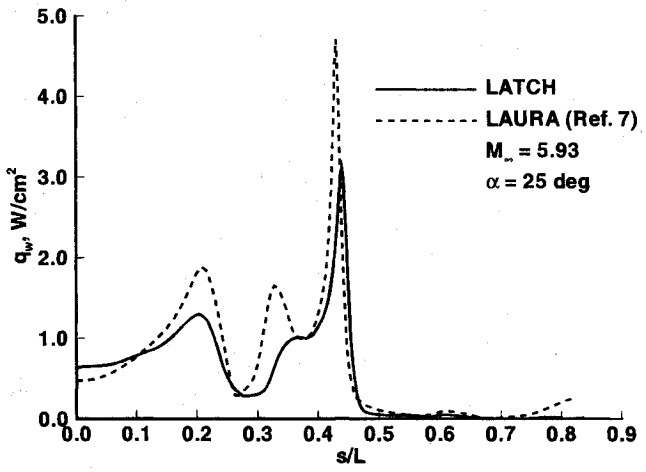

Fig. 24 Circumferential heating distribution on HL-20 at $x/L = 0.8$.

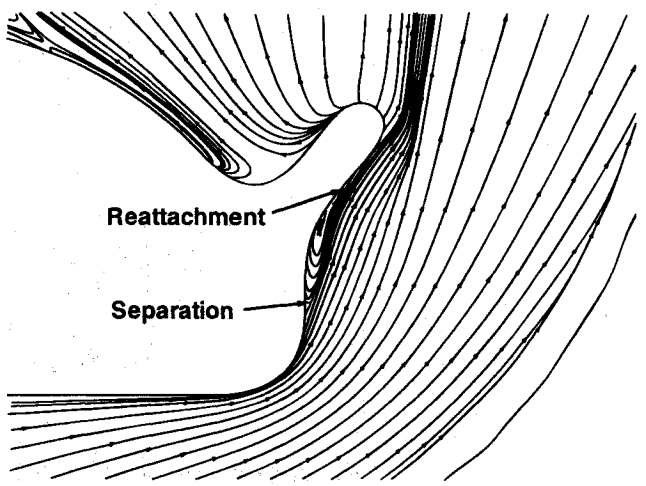

Fig. 25 Cross flow streamline pattern on HL-20 at $x/L \approx 0.7$.

reaches a peak near the edge of the fuselage lower surface; and then decreases on the side of the body as before (i.e., at $x/L = 0.2$ and 0.4). However, the protrusion of the wing into the flow causes an increase in heating and a second peak in the heating distribution. The LATCH predictions are in good agreement with the LAURA results except near the peak heating regions.

At $x/L = 0.8$ (Fig. 24), the wing is fully developed and the heating distribution undergoes a further change with the emergence of a third peak in heating. The first peak (near $s/L \approx 0.2$) is associated with the rapid divergence of the flow near the bottom edge of the fuselage, as discussed previously; the second (near $s/L \approx 0.3$) is associated with a region of crossflow separation and reattachment that occurs near the juncture of the fuselage and wing; and the third (near $s/L \approx 0.4$) is associated with the wing leading edge. The crossflow separation region at a location slightly upstream ($x/L = 0.7$) is clearly shown in Fig. 25 by the streamline pattern obtained from the LAURA (thin-layer version of Navier-Stokes) flowfield solution. The high heating near $x/L \approx 0.3$ is associated with reattachment. The LATCH predictions follow the trends of the LAURA results except in the vicinity of the second peak in heating, which is associated with the crossflow separation region. However, because the external flowfield for the LATCH calculations is inviscid and cannot predict separation, it is not surprising that the two calculations disagree in this region. In the vicinity of the other two heating peaks (near the leading of the fuselage and the wing), the LATCH predictions are lower than the LAURA calculations, as discussed previously.

The flow in the vicinity of the leading edges is highly three-dimensional, and thus the underprediction of heating by LATCH near the leading edges is probably the result of neglecting the crossflow in the boundary layer perpendicular to the inviscid streamline direction and the three-dimensional effects associated with that crossflow. However, the heating over the remainder of the vehicle, where the flow is attached, is predicted reasonably well.

Concluding Remarks

A method has been presented for calculating heating on three-dimensional vehicles at angle of attack (LATCH). The method is based on the axisymmetric analog for three-dimensional boundary layers and uses a generalized body-fitted coordinate system. Edge conditions for the boundary-layer calculations are obtained from an inviscid flowfield solution. The coordinate system used in the heating calculations is based on an inviscid flowfield grid defined in cartesian coordinates. Thus, it is possible to use this method to calculate the heating on any blunt nosed vehicle geometry for which an inviscid flowfield can be computed.

The method has been validated by comparing predicted heating rates on the HALIS orbiter with experimental wind-tunnel data (Mach 5.83, a Reynolds number of 1.9×10^6 per meter, and an angle of attack of 30 deg), calculations from a thin-layer version of a Navier-Stokes code (LAURA) and results of an earlier engineering code (AA3DBL). Comparisons were made along the windward symmetry plane and in a circumferential direction around the body at an axial station of $x/L = 0.55$. From these comparisons, it has been shown that the LATCH code gives a reasonably accurate prediction of the heating over this type of vehicle.

Heating rates from the LATCH code were also compared with calculations from a thin-layer version of a Navier-Stokes code (LAURA) on the HL-20 configuration at a Mach number of 5.93, a Reynolds number of 7.54×10^6 per meter, and an angle of attack of 25 deg. The AA3DBL code could not be applied to this configuration because it uses a much more restrictive coordinate system that breaks down in the vicinity of the wings. The comparisons were similar to those made on the modified Shuttle Orbiter and showed that the LATCH code can be used to give accurate predictions of the heating on this type of winged entry vehicle except in regions where flow separation occurs and near fuselage or wing leading edges. The underprediction of heating near the leading edges is probably the result of neglecting crossflow in the boundary layer (in a direction perpendicular to the inviscid streamline direction) in these regions where the flow is highly three dimensional.

The LATCH code has a very short run time (a few minutes on a desktop work station), and it can be applied to any vehicle geometry for which an inviscid flowfield solution can be obtained. Although the inviscid flowfield solution requires a significant amount of run time (several hours for a complex body shape), it still requires one or two orders of magnitude less time than a Navier-Stokes solution. Thus, the LATCH code combined with an inviscid flowfield code is much better suited (than a Navier-Stokes code) for use in most parametric studies associated with preliminary design.

References

[1] Hamilton, H. H., II, DeJarnette, F. R., and Weilmuenster, K. J., "Application of Axisymmetric Analog for Calculating Heating in Three-Dimensional Flows," *Jounal of Spacecraft and Rockets*, Vol. 24, No. 4, 1987, pp. 296–302.

[2] Weilmuenster, K. J., and Hamilton, H. H., II, "Computed and Experimental Surface Pressure and Heating on 70-Deg Sphere Cones," *Journal of Spacecraft and Rockets*, Vol. 24, No. 5, 1987, pp. 385–393.

[3] Cooke, J. C., "An Axially Symmetric Analogue for General Three-Dimensional Boundary Layers," Reports and Memoranda No. 3200, British Aeronautical Research Council, 1961.

[4] Weilmuenster, K. J., and Hamilton, H. H., II, "Calculation of Inviscid Flow over Shuttle-Like Vehicles at High Angles of Attack and Comparisons with Experimental Data," NASA TP-2103, May 1983.

[5] Hamilton, H. H., II, Greene, F. A., and Weilmuenster, K. J., "Comparison of Heating Calculations with Experimental Data on a Modified Shuttle Orbiter," *Journal of Spacecraft and Rockets*, Vol. 29, No. 2, 1992, pp. 208–215.

[6] Hoffman, K. A., *Computational Fluid Dynamics for Engineers*, Engineering Education Systems, Austin, TX, 1989, pp. 307–310.

[7] Gnoffo, P. A., "An Upwind-Biased, Point-Implicit Relaxation Algorithm for Viscous, Compressible Perfect-Gas Flow," NASA TP-2953, Feb. 1990.

[8] Micol, J., "Aerothermodynamic Measurement and Prediction for a Modified Orbiter at Mach 6 and 10," AIAA Paper 91-1436, June 1991.

[9] Throckmorton, D. A., and Hartung, L. C., "Space Shuttle Entry Heating Data Book," Vol. I—STS-2, NASA RP-1191, May 1988.

[10] Hamilton H. H., II, Millman, D. R., and Greendyke, R. B., "Finite-Difference Solution for Laminar or Turbulent Boundary-Layer Flow Over Axisymmetric Bodies with Ideal Gas, CF_4 or Equilibrium Air Chemistry," NASA TP-3271, Dec. 1992.

[11] Zoby, E. V., Moss, J. N., and Sutton, K., "Approximate Convective Heating Analysis for Hypersonic Flows," *Journal of Spacecraft and Rockets*, Vol. 18, No. 1, 1981, pp. 64–70.

[12] Zoby, E. V., "Approximate Heating Analysis for the Windward Symmetry Plane of Shuttle-like Bodies at Large Angle of Attack," *Thermophysics of Atmospheric Entry*, edited by T. E. Horton, Vol. 82, Progress in Astronautics and Aeronautics, AIAA, New York, 1982, pp. 229–247.

[13] Shinn, J. C., Moss, J. N., and Simmonds, A. L., "Viscous Shock-Layer Heating Analysis for the Shuttle Windward Plane with Surface Finite Catalysis Recombination Rates," *Entry Vehicle Heating and Thermal Protection Systems: Space Shuttle, Solar Starprobe, Jupiter Galileo Probe*, edited P. E. Bauer and H. E. Collicott, Vol. 85, Progress in Astronautics and Aeronautics, AIAA, New York, 1983, pp. 149–180.

[14] Thompson, R. A., "Comparisons of Nonequilibrium Viscous Shock-Layer Solutions with Shuttle Heating Measurements," *Journal of Thermophysics and Heat Transfer*, Vol. 4, No. 2, 1990, pp. 162–169.

[15] Piland, W. M., Talay, T. A., and Stone, H. W., "The Personal Launch System," *Aerospace America*, Nov. 1990, pp. 18–21, 29.